Long-term development of a perennial firn aquifer on the Lomonosovfonna ice cap, Svalbard

Tim van den Akker[1], Ward van Pelt[2], Rickard Petterson[2], Veijo A. Pohjola[2]

[1]Institute for Marine and Atmospheric Research Utrecht, Utrecht University, Netherlands

5 [2]Department of Earth Sciences, Uppsala University, Uppsala, Sweden

Correspondence to: Tim van den Akker (t.vandenakker@uu.nl)

10 **Abstract.** An uncertain factor in assessing future sea level rise is the melt water runoff buffering capacity of snow and firn on glaciers and ice caps. Field studies have resulted in observations of perennial firn aquifers (PFAs), which are bodies of water present deep in the firn layer and sheltered from cold surface conditions. PFAs can store surface melt, thereby acting as a buffer against sea level rise, and influence the thermodynamics of the firn layer. Furthermore, ice dynamics might be affected by the presence of liquid water through hydrofracturing and water transport to the bed, and such influence bed properties and

15 ice flow. In this study, we present results of applying the USGS Modular Hydrological Model MODFLOW 6 to an observed perennial firn aquifer on the Lomonosovfonna ice cap in central Svalbard. The observations span a three-year period, where a ground penetrating radar was used to measure the water table depth of the aquifer. We calibrate our model against these observations to infer a hydraulic conductivity of firn snow of $6.4 * 10^{-4}$ m s^{-1}, and then use the model to project the aquifer evolution over the period 1957 – 2019. We find that the aquifer was present in 1957, and that it steadily grew over the modelled

20 period with a relative increase of about 15 % in water table depth. On an annual basis, the aquifer exhibits sharp water table increases during the melt season, followed by slow seepage through the cold season.

1 Introduction

Aquifers, defined in groundwater analysis as an underground layer of permeable material that traps liquids in its pore spaces, can hold substantial volumes of water. Firn, defined as multi-year snow with a lower density than ice, contains pore spaces

25 and can therefore also contain water. Kuipers Munneke et al. (2014) found that aquifers can form in firn layers of ice caps or glaciers, given certain meteorological conditions. If a firn aquifer persists for multiple years, i.e. in case it does not entirely drain of refreeze in the cold season, it is referred to as a perennial firn aquifer (PFA).

PFA's can form when i) there is enough water input into the firn, either by rain or surface melting and ii) there is enough pore space at depth to accommodate the percolated water and to shelter the PFA from refreezing during (winter) cold periods

30 (Kuipers Munneke et al., 2014). Future climate warming introduces both positive and negative effects on PFA extent and

volume. On the one hand, increased (atmospheric) temperatures lead to more meltwater and/or rain as input to a PFA, and a less cold winter period reduces conductive cooling and refreezing of a PFA from above. On the other hand, higher firn temperatures lead to a denser firn pack (Brils et al., 2022; Van Pelt et al., 2019; Kuipers Munneke et al., 2014), and less firn air content or pore space (Veldhuijsen et al., 2023), lowering the potential of the firn to retain meltwater and thereby preventing volume growth of the aquifer. Regions in which PFAs are already present, such as on the Greenland Ice Sheet and Svalbard, might disappear or move up-glacier once the firn is too dense to foster a PFA.. In other areas, that where too cold for PFA formation in the past but have a deep and airy firn layer , PFA formation may be initiated. This could happen for example on the Antarctic Ice Sheet (Veldhuijsen et al., 2024).

A key requirement for PFAs to form is temperate conditions at depths $>\sim10$ m below the surface (in addition to a lack of options for the water to drain supra- and englacially via streams, crevasses and moulins). In Svalbard, temperate firn at such depths exists across nearly all accumulation zones (Van Pelt et al., 2019), and previous work has already shown PFA existence on the Holtedahlfonna ice cap (Christianson et al., 2015) and the Lomonosovfonna ice cap (Hawrylak and Nilsson, 2019). Furthermore, PFAs have been found in Greenland (Forster et al., 2014; Koenig et al., 2014) and on mountain glaciers in other Arctic regions, e.g. in Canada (Ochwat et al., 2021) or the USA (Fountain, 1989). Miller et al. (2020) found that the residence time of water in the Greenland PFA is about 6,5 years, and Poinar et al. (2017) found that aquifer flow enhanced the formation of deeper crevasses. Recently, surface melt water streams have been identified on the Antarctic ice sheet that are said to be able to form firn aquifers (Kingslake et al., 2017). Modelling studies have already shown that perennial firn aquifers can form on the Antarctic peninsula (Van Wessem et al., 2021) and on the rest of the Antarctic Ice Sheet (Van Wessem et al., 2020). Radar observations of an East Antarctic outlet glacier indicate the possible presence of a PFA, comparable to the one found on the Greenland ice sheet (Lenaerts et al., 2017; Lenaerts et al., 2018; Schaap et al., 2020).

Previous efforts have been made to model the formation and development of PFAs. Kuipers Munneke et al. (2015) present a one-dimensional aquifer model, which is designed to assess under what climatic conditions an aquifer will form, and how wet firn responds to climate change, compared to dry firn. Whereas previous efforts have primarily focused on simulating vertical meltwater percolation (Marchenko et al., 2017a; Steger et al., 2017; Vandecrux et al., 2020), attempts to model water flow in PFAs are scarce. Recently, Miller et al. (2023) modelled a PFA on Helheim glacier in Greenland using SUTRA-ICE, a 2D model combining groundwater flow with a subsurface energy balance model to calculate freeze-thaw cycles. The model SUTRA-ICE is comprehensive: it contains water flow through the unsaturated zone as well as water movement within the saturated zone. Freeze-thaw cycles are modelled, so potential winter refreezing of (a part of) the modelled PFA is included. The model is tested on a two-dimensional flowline of Helheim glacier, with constant recharge rates. Three-dimensional flow and realistic meltwater input from a (downscaled) climate or energy balance model is missing. For an extensive comparison of firn models and their components, the reader is referred to Vandecrux et al. (2020) and Stevens et al. (2020).

A key parameter needed to accurately model a PFA is the hydraulic conductivity of firn and snow, being the main control on water flow rates. Fountain and Walder (1998) examined field tests of five different glaciers and found a range of $1 - 5 *10^{-5}$ m s^{-1}. They argue that firn conditions are therefore uniform between glaciers, because of the low range in measured hydraulic conductivity. Miller et al. (2017) did slug tests on the Greenland Ice Sheet (GrIS) and found hydraulic conductivities ranging between $2.5 *10^{-5}$ m s^{-1} and $1.1 *10^{-3}$ m s^{-1}. Stevens et al. (2018) found in their literature review a range of $10^{-6} - 10^{-2}$ m s^{-1}, using similar techniques as Miller et al. (2017) on ten northern hemisphere glaciers (in Canada, Svalbard, northern Sweden, Greenland and the Alps).

In this study, we combine three years of field data (2017-2019), a state-of-the-art firn model and a 3D groundwater-flow model to simulate the evolution of a PFA found on the Lomonosovfonna ice cap on Svalbard from 1957 - 2019. We approach the PFA as a classical groundwater system of flow through a porous medium, with meltwater input at the top and outflow through the boundaries. Surface and firn processes such as melt, water percolation, refreezing, heat diffusion and firn densification are resolved by the Energy Balance Firn Model (EBFM; Van Pelt et al. (2019)), which provides input to the PFA model. The PFA model is calibrated using the hydraulic conductivity, pore close-off depth and seepage rate to fit with in situ observations of three consecutive years, obtained with ground-penetrating radar (GPR) measurements. Our objective with this work is to add to the knowledge of the dynamics of firn aquifers, and in particular how changes in the aquifer can be described numerically by a hydrogeological model. Furthermore, the modelling gives a long-term perspective of how the thermal regime and water storage have changed on an Arctic ice cap since the 1950s.

2 Study area

The Lomonosovfonna ice cap is situated in central eastern Spitsbergen, the largest island of the Svalbard-archipelago, see Fig. 1. It is the highest ice cap of Svalbard, reaching up to 1250 m a.s.l. The Lomonosovfonna ice cap is about 600 km^2, and feeds into several outlet glaciers. Two of these outlet glaciers, Tunabreen and Negribreen, have surged over the last 20 years (Flink et al., 2015; Haga et al., 2020; Koch et al., 2023). Nordenskiöldbreen and the Lomonosovfonna ice cap are monitored since 1997 by Uppsala University and Utrecht University (Marchenko et al., 2019; Marchenko et al., 2017b; Marchenko et al., 2021; Van De Wal et al., 2002). The monitoring program consists of mass balance monitoring, ice velocity measurements, ice thickness measurements and meteorological observations. A map of the Lomonosovfonna ice cap, showing the locations where the observations were done, is presented in Figure 1b. Previous glaciological studies, using the data from the monitoring program, on Nordenskiöldbreen and the Lomonosovfonna ice cap have assessed climatic mass balance (Van Pelt et al., 2012), snow and firn conditions (Marchenko et al., 2019; Marchenko et al., 2017a; Pohjola et al., 2002) and ice dynamics and thickness (Van Pelt et al., 2013; Van Pelt et al., 2018). The modelled grid in this study, together with the areas where GPR observations were made per year, is shown in Figure 1b (light blue box).
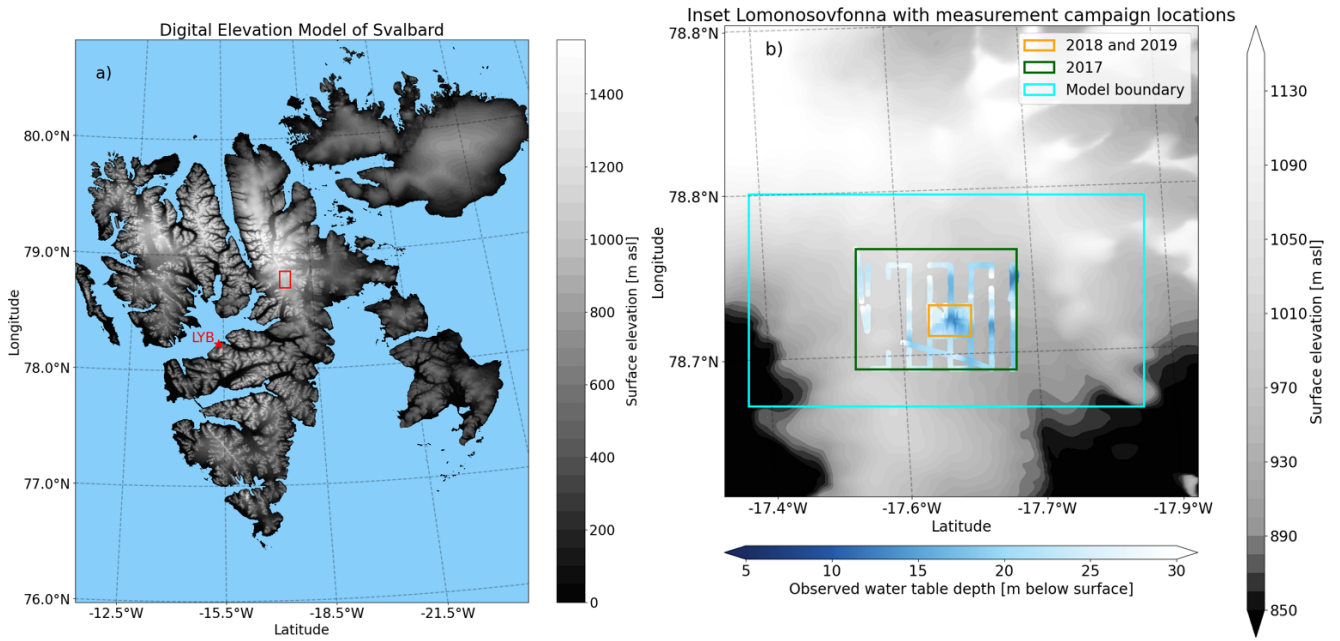
Figure 1 (left). The Svalbard archipelago, plotted from the digital elevation of the Norwegian Polar Institute (2014) model of with Longyearbyen airport (LYB) shown with a red star. The red rectangle in the left figure shows the inset shown on the right, which is the location of the water table observations over the years 2017 (green), 2018 and 2019(orange, same location in both years). The rectangles correspond to the minimum and maximum coordinates of the observations in those years and thus show the extent of the PFA measurements. The model boundary in this study is shown in cyan, with a buffer zone around the observation campaign, The datapoints obtained in these campaigns are turned to water depths (using the methods described in the next paragraph). The datapoints and extent of the observation campaign of the years 2018 and 2019 are nearly identical and therefore overlap.
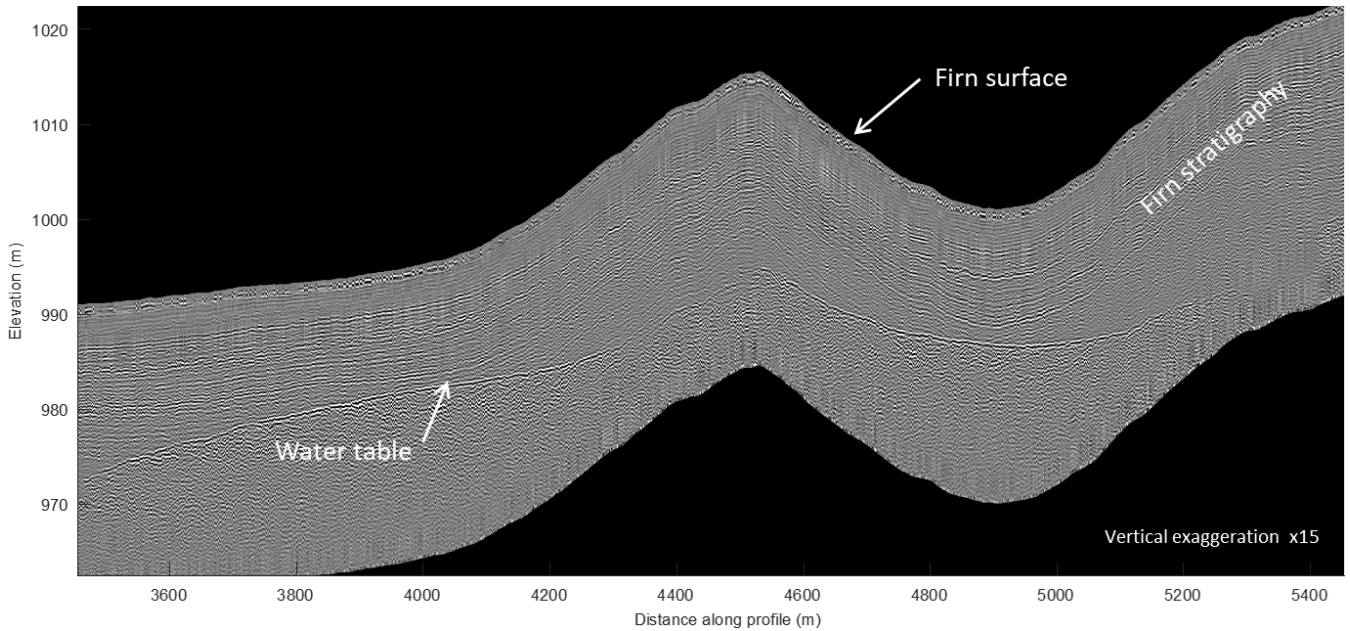
3 Data and methods

3.1 Water table height data

We use water table depth observations obtained at the Lomonosovfonna ice cap as our main tuning data for the ground water flow model. The water table depth was obtained from ground penetrating radar data, where the water table stands out clearly due to the large permittivity difference between liquid water and air-saturated firn (Fig. 2). The GPR data was collected with a Malå ProEx radar system with a 250 MHz antenna pulled behind a snowmobile. The positioning of the radar profiles was done with a two-frequency geodetic GNSS receiver. The GPR profiles followed a grid pattern over the study area (Fig. 1) and were collected during March-April in 2017, 2018 and 2019. The average length of the radar profiles during one season is ~40 km.

4

110   The raw GPR data was minimally processed with zero-time adjustment and a low-pass filter (300 MHz cut-off frequency). An example radargram is shown in Fig. 2. The water table is semi-automatically picked from a radargram (example in Fig. 2). First, the reflective surface of the water table is manually found in a single data point. Next, a tracing algorithm is used to track the reflective surface through adjacent points. This results in the two-way travel times (TWTT) per datapoint. Then, the velocity of the radar wave in the firn is used to calculate the distance to the water table from the surface. For this, the dielectric constant

115   of firn is required, which is calculated according to Kovacs et al. (1995) where ρ_f is the density of the firn layer and ρ_w the density of water:

$$\epsilon_f = \left(1 + 0.845 * \frac{\rho_f}{\rho_w}\right)^2 \tag{1}$$

Figure 2: An example of a topographically corrected (x15 exaggeration) radargram. The water table of the firn aquifer is clearly visible and

120   cuts the general firn stratigraphy. The resulting observed water table depth is shown in Fig. 1.

The density of the firn ρ_f at the location of the observations is obtained from the Energy Balance Firn Model (EBFM; Van Pelt et al., 2019), of which a description is given in the next section.

125

3.2 Water input & firn density from the Energy Balance Firn Model

5

In this model study, time-dependent firn density and meltwater input are the primary input variables used to model the PFA found at the Lomonosovfonna ice cap. This is retrieved from the Energy Balance - Firn Model (EBFM) (Marchenko et al., 2019; Van Pelt and Kohler, 2015; Van Pelt et al., 2012). Here, we use output from the model version of the EBFM presented
130   in Van Pelt et al. (2019), which has previously been calibrated and validated against stake measurements, weather station data and observed firn density profiles from shallow firn cores. For more details, we refer to Van Pelt et al. (2019) and references therein. A summary of EBFM components that are most relevant for this study is given below.

EBFM first solves the surface energy balance equation:

$$Q_{melt} = SW_{net} + LW_{net} + Q_{sens} + Q_{lat} + Q_{sub} \qquad (2)$$

135   Energy fluxes at the surface that are part of this model are net shortwave radiation flux (SW_{net}), net longwave radiation flux (LW_{net}), turbulent heat exchange flux through latent and sensible heat (respectively Q_{lat} and Q_{sens}), and the conductive heat flux into the ice (Q_{sub}). Equation 2 is solved for the surface temperature with a melt energy flux (Q_{melt}) set to zero. If the resulting surface temperature is higher than 0 °C, the surface temperature is set at 0 °C and the energy fluxes in Eq. 2 are recomputed, resulting in a value for $Q_{melt} > 0$. The EBFM requires air temperature, pressure, relative humidity, cloud cover and
140   precipitation as input to solve the surface energy balance, which comes from downscaled Norwegian Hindcast Archive (NORA10) regional climate model dataset (Haakenstad et al., 2020)

Below the surface, the EBFM solves the thermodynamic equation and the densification equation. The thermodynamic equation, in which ρ is the firn density, $c_p(T)$ the temperature-dependent heat capacity of the firn, κ(ρ) the firn density dependent
145   effective conductivity of the firn, F the refreezing rate (in kg m^{-3} s^{-1}) and L_m the latent heat of melting ice (3.34 x 10^5 J kg^{-1}), describes the temporal change of the temperature-depth profile due to heat conduction and refreezing of percolating and stored melt and rain water.

$$\rho c_p(T)\frac{\delta T}{\delta t} = \frac{\delta}{\delta z}\left(\kappa(\rho)\frac{\delta T}{\delta z}\right) + FL_m \qquad (3)$$

The densification equation describes the change of firn density of the firn due to gravitational compaction and refreezing.

$$\frac{\delta \rho}{\delta t} = K_g(\rho, T) + F \qquad (4)$$

The firn density of fresh deposited snow is fixed at 350 kg m^{-3}. The symbol F denotes the refreezing rate in kg m^{-3} s^{-1}.
150   Gravitational compaction $K_g(\rho,T)$ follows Ligtenberg et al. (2011):

$$K_g(\rho, T) = C(b)bg(\rho_{ice} - \rho)\, exp\left(-\frac{E_c}{RT} + \frac{E_g}{RT_{avg}}\right) \qquad (5)$$

in which C(b) is an accumulation dependent parameter (Ligtenberg et al., 2011), b the accumulation rate, ρ_{ice} is the density of ice (typically 917 kg m^{-3}), E_c is the activation energy of creep by lattice diffusion (typically 60 kJ mol^{-1}), E_g is the activation energy of gain growth (typically 42.4 kJ mol^{-1}), R is the gas constant, T is the temperature of the firn, and T_{avg} is the temporal mean subsurface temperature.

155 Water in the EBFM originates from surface melt and rain, and percolates down from the surface into the firn. This happens in two ways: by using the fast deep percolation statistical parameterization from Marchenko et al. (2017) for the instantaneous vertical distribution of available melt and rain and by applying the 'tipping bucket' scheme for subsequent vertical transport. The fast percolation instantaneously distributes water in the vertical model according to a normal distribution with a peak at the surface. Further water transport is modelled with a tipping-bucket approach. First, the water refreezes when the conditions

160 in a model layer are sufficient, being that the temperature is below melting point and the firn density below the firn density of ice. Refreezing raises the temperature and firn density. In case not all water refreezes, a small portion will be stored in the layer as irreducible water content. The remaining water will percolate down to the next layer, where the process repeats. This continues until the water encounters impermeable ice, in which case the water becomes runoff (i.e. water input in the LPFAM).

3.2 Firn aquifer modelling

165 The US Geological Survey (USGS) Modular Hydrological Model MODFLOW 6 is chosen in this research to model the horizontal and vertical water flows in the PFA on the Lomonosovfonna ice cap. For an extensive documentation, the reader is referred to (Bakker et al., 2016; Langevin et al., 2017).

Liquid flow in porous media is governed by Darcy's law, which states that a liquid will flow from areas with a higher water

170 table height towards areas with a lower water table height. It is found experimentally by Miller et al. (2020), by using salt injection in boreholes in an aquifer on the Greenland ice sheet, that water flow in a firn aquifer generally obeys Darcy's Law and can therefore be approached as a groundwater flow problem. The simplest form of the Darcy equation is given in equation 6, in which q is the flow per unit area [m s^{-1}], k the hydraulic permeability [m^2], μ the dynamic viscosity of the fluid [Pa s] and ∇p the pressure gradient vector [Pa m^{-1}].

$$q = -\frac{k}{\mu}\nabla p \qquad (6)$$

175 The hydraulic permeability is a measure of how easy a fluid moves through a medium. A higher k indicates less resistance from the medium to the flow. Often, hydraulic conductivity and hydraulic permeability are interchangeably used. Hydraulic

conductivity and hydraulic permeability are linked in Eq. 7, in which K is the hydraulic conductivity, k the hydraulic permeability, ρ the firn density of the fluid, g the gravitational acceleration, and μ the viscosity of the fluid.

$$K = \frac{k\rho g}{\mu} \tag{7}$$

Equation 6 assumes that the hydraulic permeability remains spatially constant, and all sources and sinks of the water are summarized in the ∇p term. A more comprehensive Darcy equation, adapted from Langevin et al. (2017), is:

$$\frac{\delta}{\delta x}\left(K_{xx}\frac{\delta h}{\delta x}\right) + \frac{\delta}{\delta y}\left(K_{yy}\frac{\delta h}{\delta y}\right) + \frac{\delta}{\delta z}\left(K_{zz}\frac{\delta h}{\delta z}\right) = \text{SS}\frac{\delta h}{\delta t} + Q_S \tag{8}$$

The first three terms on the left-hand side of Eq. 8 represent the flow due to differences in water table height, with a spatially varying and direction-dependent hydraulic conductivity. Q_S represents different sources and sinks, such as surface runoff, evapotranspiration, wells and precipitation. Note that those sinks and sources can be space- and time-dependent. The SS term on the right-hand side refers to specific storage, which is the water released or stored per drop of head from the pore storage. K_{xx}, K_{yy} and K_{zz} are the hydraulic conductivities that control the speed of the water flow in respectively the x, y and z direction.

The standard packages that regulate the firn density are time independent in MODFLOW 6, which means that density of the modelled medium typically does not change during a (regular) MODFLOW simulation. In groundwater modelling, with for example solid porous media like rocks and sand, this can be a justifiable simplification. This is, in the case of modelling a PFA, not desired, as the firn density changes significantly during a multi-decadal simulation.

It is therefore needed to make separate MODFLOW iterations every time step the steady packages need to change. To connect these separate MODFLOW iterations into one model, the head heights of run t are used as initial conditions for run t+1. This makes the model slower compared to a default MODFLOW 6 run. However, all runs in this study take approximately 3 hours to run on a single processor (approximately 60 model years with weekly resolution). A schematic overview of the modelling process is presented in Fig 3.
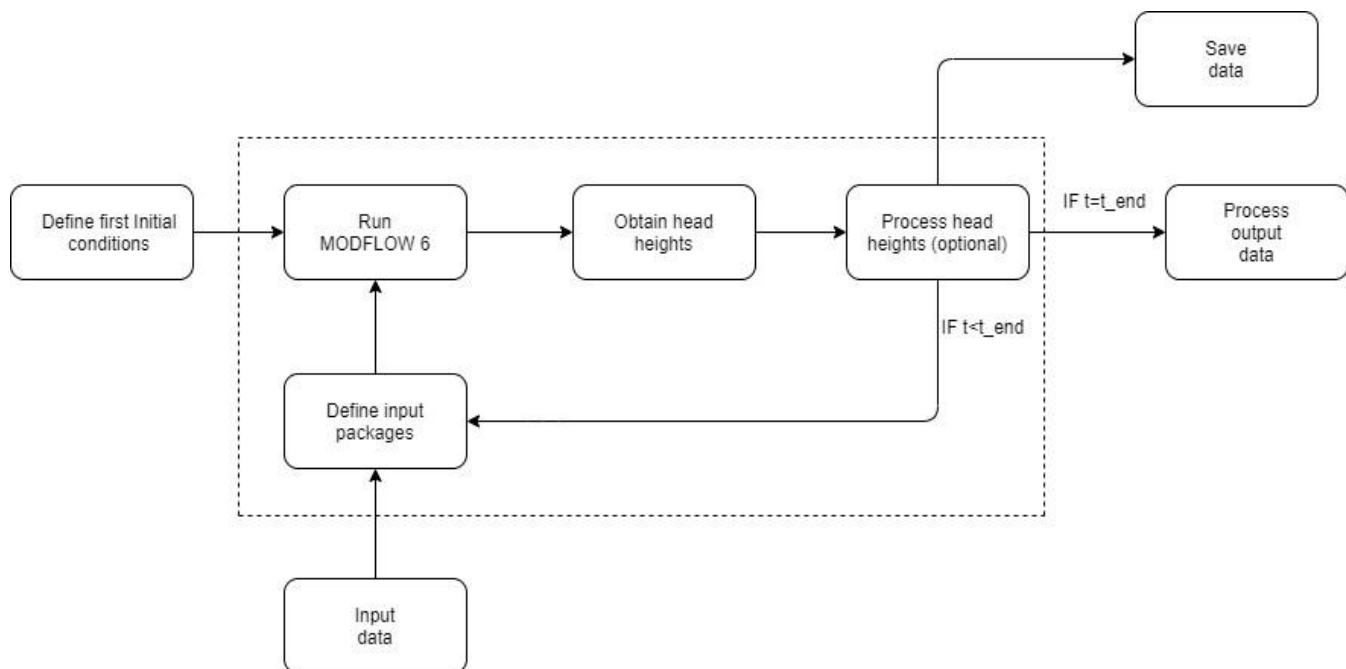
195

Figure 3: The modelling process, in which every time step a new MODFLOW model is used, using the water table height from the previous time step as initial conditions. The dotted lines indicate the loop, for which every loop is a new MODFLOW model, that uses the head height output of the previous loop as initial conditions. Note that input data can be read in every loop, instead of all at once, and that output data can be stored after each loop.

200 We run the Lomonosovfonna Perennial Firn Aquifer Model (LPFAM) on a grid of 100 by 100 cells, with 96 meters resolution in the y-direction and 72 meters in the x-direction. The vertical grid consists of 5 layers with a thickness of respectively 1.4, 3.8, 10, 24.8, 49.8 m each. Average densities for the vertical layers are extracted from the EBFM output. The water table height is resolved on a continuous vertical scale, providing more spatial (vertical) detail. We choose the model domain such that it extends several kilometres beyond the largest observational grid (2017, see Fig. 1) and that the areas with the most datapoints

205 (2018 and 2019) are roughly in the middle of the grid. This reduces the effects of the lateral boundary conditions. At the start of a spin-up routine, we fix the water table height at 10 meters above the bottom of the deepest model layer at the boundaries. This is the approximate depth at which the firn density reaches the density of glacial ice.

We performed a spin-up of 20 years, where we run 1957-1977, with in 1957 an arbitrary initialized state of 10 meters water

210 column above the bottom of the model domain. The resulting water table profile at the end of spinup (in 1977) is used as initial condition for historical runs from 1957 to 2019. We manually tune uncertain parameters to match the GPR observations in the years 2017 – 2019, as described in the next section. When changing parameter values, spin up is always repeated.

4 Results & Discussion

4.1 Model calibration & inference of hydraulic properties

In this study, three steps were performed to tune the LPFAM to reproduce a water table close to observations in the years 2017-2019. Three uncertain parameters were manually optimized, starting with the parameter K (hydraulic conductivity), to which water table height was found to be most sensitive. Remaining errors of the modelled water table versus observations are quantified by calculating the RMSE and bias.

First, we took a vertically and horizontally uniform hydraulic conductivity and we varied it between $10^{-5} - 10^{-3}$ m/s in 100 steps. The found uniform hydraulic conductivity is referred to as K_u. In a next step, a pore close-off depth is introduced. Below the pore close-off depth porosity is low causing water to be immobile (Humphrey et al., 2021; Koenig et al., 2014). We varied the pore close-off depth on a layer basis: we tried putting the close-off depth at the 5th, 4th and 3rd layer. However, it is still expected that the water can dissipate with an unknown rate from this layer, for example by entering crevasses, or by slow horizontal flow. This process is not explicitly modelled, so the pore close-off hydraulic conductivity is used as a final tuning parameter. We varied the pore close-off hydraulic conductivity to be between $10^{-1} - 10^{-6}$ times the hydraulic conductivity found in the first tuning step. The found pore close-off hydraulic conductivity is referred to as K_c. The optimal set of parameters is presented in Table 1. A summary of performance statistics for the years with observations is shown in Table 2. On average we find an average close-off firn density of 804 kg m^{-3}, happening at an average depth of 52.9 m below the surface. Our pore close-off firn density is well within the range of field studies (Gregory et al., 2014) and other modelling studies (e.g. (Huss, 2013; Ligtenberg et al., 2011; Brils et al., 2022; Herron and Langway, 1980), that typically fix the pore close-off firn density at 800-830 kg m^{-3}. Our hydraulic conductivity is also in the range of 1 * 10^{-3} - 1 * 10^{-5} [m s^{-1}] found by Miller et al. (2020); Miller et al. (2023); Miller et al. (2017) and Stevens et al. (2018).

Table 1. Optimal values found in the three consecutive tuning steps

Steps	Optimal value	Range tested and steps used
Step 1: Tuning the uniform hydraulic conductivity K	6.4 * 10^{-4} [m s^{-1}]	1 * 10^{-3} - 1 * 10^{-5} [m s^{-1}], in 100 steps
Step 2: Pore close-off depth	Layer 5	Layers 5,4,3
Step 3: Hydraulic conductivity below pore close-off depth	K (step 1) * 10^{-2}	10^{1}-10^{-10}, in 10 steps

4.2 Validation of modelled water table depth

Figure 4 show the modelled water table depth and the comparison with observations, for the three observation years (2017-2019). The LPFAM maximum vertical depth (~50 m, dependent on the thickness of the firn package) is deeper than what the GPR can observe (up to ~40 m). All radar observations with no detected water table are excluded from the comparison and cause interruptions in the tracks in Fig. 4, which hence does not mean that the water table is absent.

In 2017, observations covered the largest area (Fig. 1b). The modelled water table depth is overestimated in the southeastern corner of the grid. Although the modelled and observed spatial variations are comparable (R = 0.68), the LPFAM has a water table significantly closer to the surface (bias = 2.3 m). This could be because there are missing sinks in the LPFAM in that region. During observational campaigns, the GPR could not measure beyond the southwestern corner because of the presence of a crevasse field, see for example Hawrylak (2021). These crevasses could very well act as a sink that is currently unaccounted for in the model. As a result, the root-mean-square error (RMSE) is significantly larger for the large grid observed in 2017 (5.05 m) than for the small grid in 2018 (1.03 m) and 2019 (1.49 m), where vertical drainage is likely small or absent.

The modelled water table depth height agrees very well with the in situ observations on the smaller grid during the years 2018 (RMSE = 1.03 m, bias = 0.5 m, R = 0.97, maximum error: 3.2 m) and 2019 (RMSE = 1.49 m; bias = 1.23 m; R = 0.97, maximum error: 4.3 m). Within the observation grid in 2018 and 2019 (Fig 4), the northwestern, southwestern, and northeastern corners contain little water according to model and observations, whereas water flow is steered by the surface topography to the flatter central part and southeastern corner, before leaving the observational grid .

In Fig. 5, the modelled water table depth and the nearest observed water table depth are compared. The modelled water table depth patterns in 2018 and 2019 correlate very well with the observations (Table 2). In 2017, the outliers in the modelled water table depth are mostly below the 1:1 line i.e. the modelled water table depth is locally underestimated, i.e. water table height is overestimated, compared to the observations, confirming the missing sinks in the southwestern corner of the model grid. Adding sinks would lower the modelled water table height and possibly remove the outliers.

From the height contours and water table height pattern it can be inferred that water table height variations are steered by surface topography, rather than lateral firn density variations. Locally elevated (convex) areas are often modelled and observed to have a deeper water table, whereas local depressions (concavities) in the terrain are associated with a water table close to the surface. This applies to both the smaller grid (2018 and 2019) and the larger grid (2017).
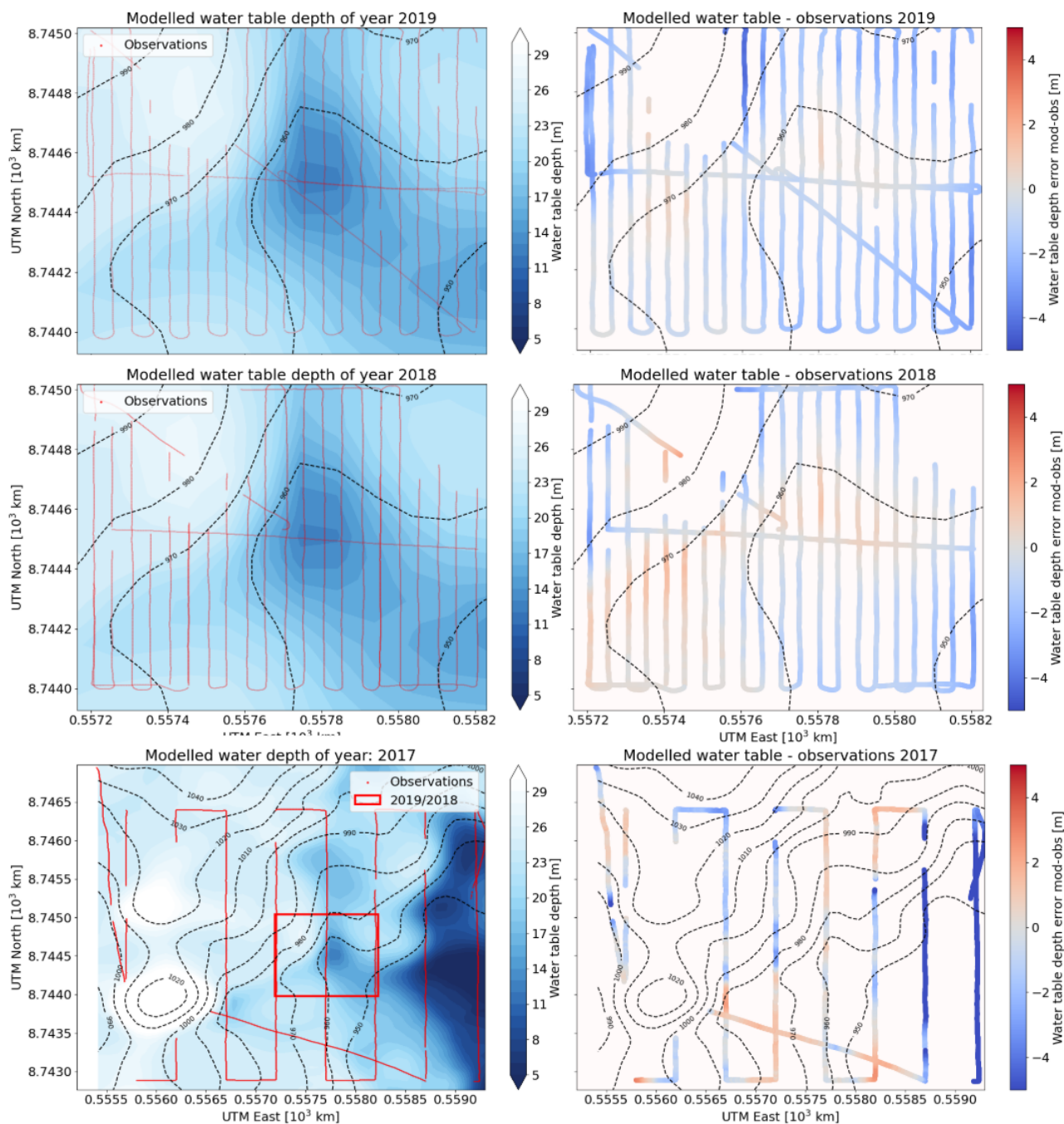
Figure 4. Modelled water table depth and the difference wrt to observations (left column) modelled water table depth for the years with the most observational coverage (2017,2018,2019). The observational data point locations are shown in red. The surface height contours, taken from the NPI DEM per 10 m a.s.l. are shown with black dashed lines. (right column) Modelled water table depth minus observed

water table depth, where modelled values are interpolated to the locations of the observations. The performance statistics are shown in Table
275   2. In the bottom left panel the studied area in 2018 and 2019 is marked by the red rectangle.

Table 2. Performance indicators of the perennial firn aquifer depth from the model and compared to observed firn aquifer depth. The RMSE and bias are determined by comparing all modelled points within the observational grid of a given year with the closest observed location. This results in 145, 143 and 835 datapoints respectively in the years 2019, 2018, and 2017. The mean modelled and mean observed depths
280   are the arithmetic means of the aforementioned matched data points

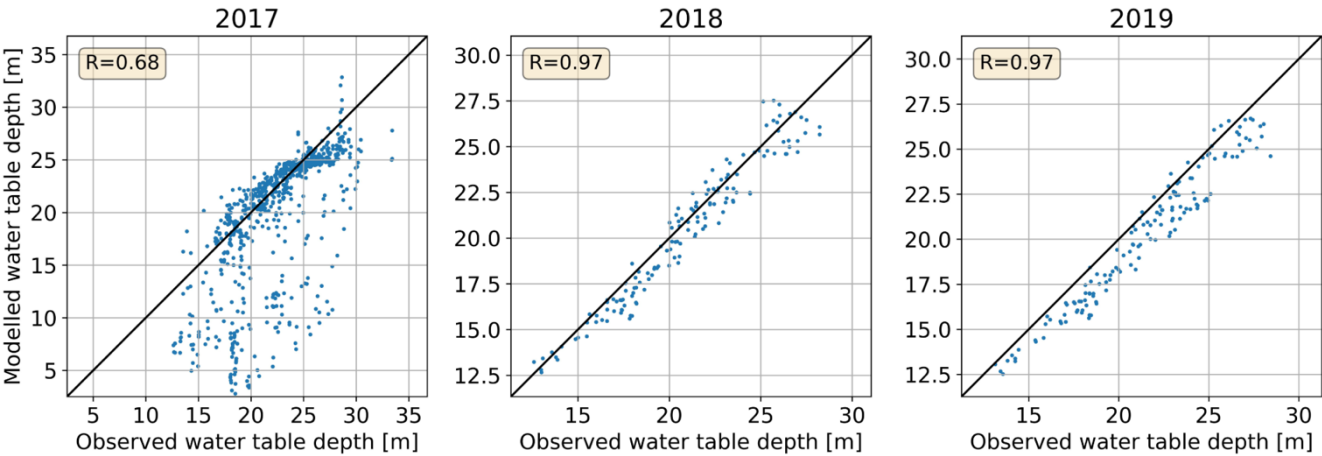| Year	Mean modelled PFA depth [m]	Mean observed PFA depth [m]	RMSE [m]	Bias [m]	Correlation R [-]	P-value [-]
2019	20.2	21.4	1.49	1.2	0.974	< 0.001
2018	20.3	20.8	1.03	0.5	0,972	< 0.001
2017	20.3	22.6	5.05	2.3	0.678	< 0.001

Figure 5. Scatter plots of the modelled and observed water table depths in 2017 (left), 2018 (middle) and 2019 (right). The black line is the 1:1 line, and the calculated correlation is shown in the top left corner of each panel.

285

4.3 Multidecadal PFA development

At the end of our spin-up routine in 1977 a PFA is present in the firn. The timeseries in Nordli et al. (2020) show homogenised observational timeseries for Svalbard (Longyearbyen) back to 1898. Fig. 3 in Nordli et al. (2020) reveals that the decades
290   before 1957 (~1930-57) were warmer than the period 1957-1977. Even though these timeseries apply to sea level we argue it is unlikely that an opposite temperature trend applies at high elevations. Since we used the colder period 1957-1977 to initialize

13

our model, the presence of a perennial firn aquifer at the end of the spin-up period is a strong indication that a perennial firn aquifer would also have been present in 1957. We argue that higher temperatures imply more surface melt and likely growth of the PFA (assuming snow accumulation does not drop markedly during warm periods). Fig. 6 confirms that warm (high melt) years typically induce an increase in water table height. Furthermore, high melt (and accumulation) rates were also listed as a requirement for firn aquifer formation in Kuipers Munneke et al. (2014). Based on the likely warmer temperatures prior to 1957 than the period that was used for model spin-up, we argue that the perennial firn aquifer may have been larger than the size it currently has at the start of the simulation in 1957.

It is worth noting that initial PFA water table depth perturbations only affect simulated water table depths in the first 10-20 years, which is the typical response time of the PFA. However, when starting a simulation with no perennial firn aquifer, we find an unphysical increase in water table depth even during the cold season for the first ten years of the simulation (not shown). This modelled behaviour and the temperature dataset of Nordli et al. (2020) makes it very likely that the PFA was already present well before 1957.

The water table height at a central location in the model domain is plotted together with the meltwater input from the EBFM for the whole run and for the last years in Fig. 6. There is in general a positive trend, both in modelled average water table depth and meltwater input. It can clearly be seen that the PFA reacts quickly to a meltwater input peak. There is a time delay between a peak in meltwater input and aquifer water table height in the order of weeks. This delay is likely caused because this location is in the centre of a topographic low. It can therefore receive water from all sides, which extends the growing phase of the aquifer in this location beyond the initial pulse. The strongest meltwater peaks coincide with sharp water table height increases. Once the water table depth peak has passed, the water table decreases again with a rate dependent on the peak magnitude but following the same smooth pattern every year. Large rapid jumps in the water table height occur during high-melt summers, such as in 1998 and 2016, while gradual decreases of the water table height occur during multiyear cold periods, e.g. 1962-1966 or 1994-1997.
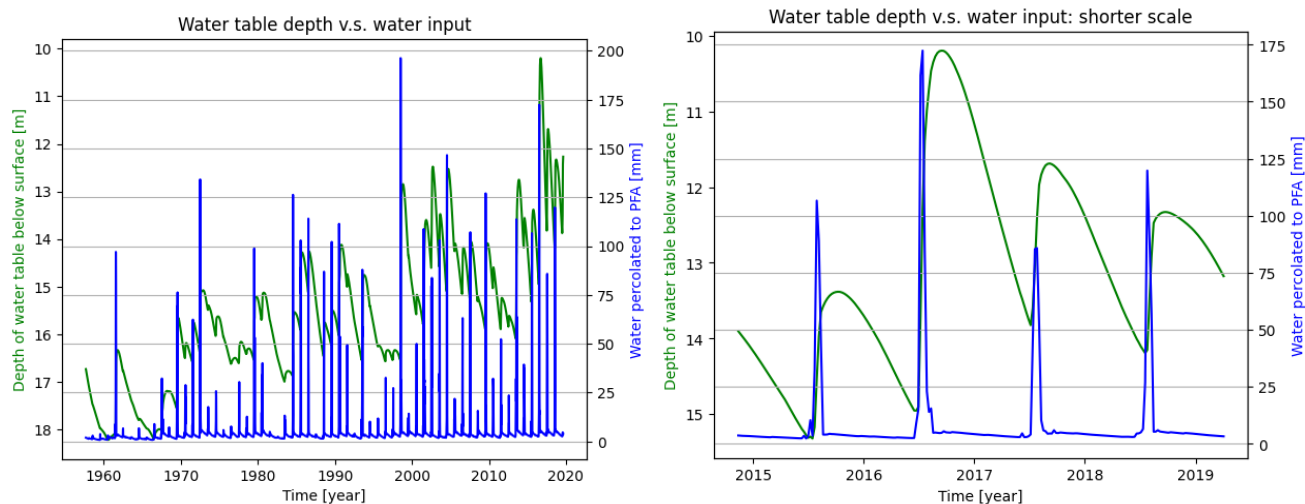
14

Figure 6. Water table depth from LPFAM versus meltwater input from EBFM for the whole simulation (left) and for the final years (right).
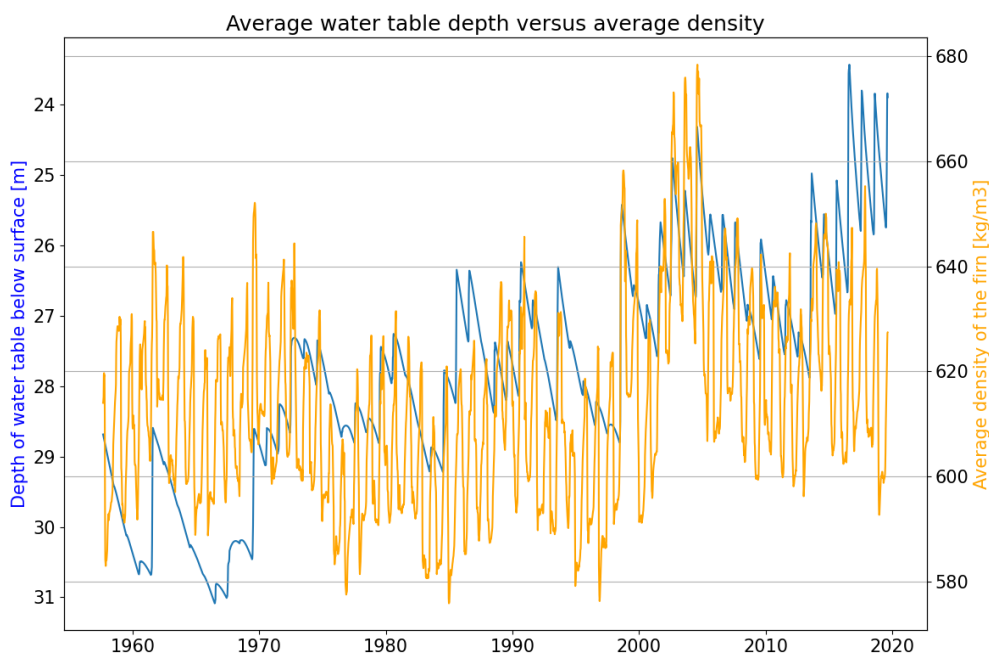

320

Figure. 7 Average density of the firn from the EBFM (orange) with the average water table height from the LPFAM (blue).

15

In Fig. 7, the average firn density on the model grid versus the average water table depth (for the whole model grid) is shown. The R-correlation between water table depth and average firn density is -0.41 (negative, as a higher firn density

325 corresponds to a lower water table depth). Firn compaction hence contributes significantly to the modelled increases in water table height, although most of the water table height variations are related to the total water content (R=-0.75).

4.4 Uncertainties

Although LPFAM captures the main processes to describe PFA formation and development, some processes or interactions are not accounted for thereby inducing uncertainties. A main source of uncertainty is that there is only a one-way coupling

330 from EBFM to LPFAM. Two-way coupling would be more physically desirable. For example, the extra weight of water in saturated firn will induce faster densification by the gravitational overburden pressure, a process currently not incorporated in the EBFM. Furthermore, as soon as the aquifer reaches closer to the surface, the overlaying firn may not be able to protect the water from refreezing. The observed water table does not get closer than 10 metres below the surface, so for the present-day conditions this is unlikely to happen. However, in the future, with less pore space and more meltwater production refreezing

335 of the water table might occur. Meltwater refreezing creates an ice layer in the firn. This ice lens, when thick enough, can impede free vertical movement of the water table and prevent meltwater from the surface to reach the aquifer. Hence, under such conditions the PFA is no longer entirely unconfined. A two-way coupled EBFM - LPFAM, where on top of the current couplings, refreezing of PFA water and densification of saturated firn are accounted for, could be the scope of future work.

Another source of modelling errors is vertical water drainage through local sinks, such as crevasses and moulins, which is not

340 accounted for. Instead, all water drains through the lateral boundaries of the grid. No data is available on the existence, location, size and capacity of the sinks within our modelled grid on Lomonosovfonna, so they could not be incorporated in the LPFAM. The only sink for water in the LPFAM is horizontal movement through the boundaries of the model domain. As can be seen in the results for 2017, the LPFAM overestimates the water table height in the southeastern corner of the model grid. There is likely a crevasse field there, but we do not know the specific locations and dimensions of the crevasses. Also, the interaction

345 between the aquifer and crevasses, in particular the drainage rates, are unknown. Preliminary tests with artificial drains with almost instant drainage in 40 grid cells position north – south 50 meters East of the of the observation grid improved the results (RMSE decreases from 5.05 m to 3.24 m in 2017, from 1.03 m to 0.89 m in 2018 and from 1.49 to 1.10 in 2019). Identification of crevasse fields in satellite products, e.g. Sentinel-1 or Sentinel-2, is challenging in accumulation zones, but could provide important data on PFA sinks in the area.

350 There are uncertainties in the observed water table depth shown in this study. The system specific uncertainty (related to the sampling frequency, the cable length, and the GPR used is small and about ±0.02 meters. The largest source of uncertainty stems from the calculation of the velocity of the radar wave, which is calculated using a modelled density profile of the firn. When changing the firn density arbitrarily with ±10%, this resulted in a spread of ±0.21 m in calculated water table depths.

The uncertainty arising from digitizing the water table, quantified by doing cross analysis of double-measured points during the same field season, results in ±0.03 m.

In a future climate, increased melting and rainfall (Hansen et al., 2014; Bintanja and Andry, 2017) will lead to less deep and higher firn densities, and will lead to a water table depth that reaches closer to the surface. This will simultaneously increase the likelihood for wintertime freezing of the water table in places where the water table is close enough to the surface (<8-10 m). During the modelled period (1957-2019) this has not occurred yet, as water table depth did not reach closer than 12 m below the surface in the observations. In 2012 and 2013. The firn temperature at the Lomonosovfonna ice field has been measured with thermistor strings, and the cold wave did not penetrate to below approximately 10 meters (Marchenko et al., 2017b). For the future development of the PFA, this could become important, as well as the formation of surface streams or meltwater lakes, if the surface topography allows for it

The hydraulic conductivity we find by calibrating the LPFAM ($6.4*10^{-4}$ m s^{-1}) is in between the values of 10^{-5} - 10^{-3} m s^{-1} (Fountain and Walder, 1998; Miller et al., 2020; Miller et al., 2023; Miller et al., 2017; Stevens et al., 2018). We find this uniform hydraulic conductivity by manually tuning our model until it fits with observations. A tuned variable can only represent a real parameter if all other process at play are perfectly represented, so our tuned variable can compensate for errors in the firn conditions from the EBFM, uncertainties in observations and/or missing processes. Furthermore, the hydraulic conductivity of horizontal water flow above the pore close-off depth is assumed to be a constant in this study, but in reality likely depends on the porosity of the firn. In future work, the porosity dependence of hydraulic conductivity could be inferred using a higher (vertical) resolution PFA modelling, more extensive water table depth data, borehole pressure data, and/or pump or slug tests.

5. Conclusions

In this study, we adapted an existing groundwater flow model MODFLOW6 so that it can be applied to model a perennial firn aquifer. We test the model setup on a PFA, that has been observed on the Lomonosovfonna ice cap in central Svalbard. We use in situ measurement campaigns of three consecutive years to tune uncertain parameters, so that the modelled water table height fits with observations. From the calibration we infer a hydraulic conductivity of the PFA of $6.4 * 10^{-4}$ m s^{-1}. After spin up, we run the PFA model from 1957 – 2019 and find a general increase in water table height over the modelled period, with large jumps during high melt summers. We find that the PFA likely already existed before 1957. The height of the water table reacts quickly to meltwater input, in the order of weeks, and long-term water table depth variations further depend on long-term firn density changes. During the cold season, the water table decays steadily to a minimum prior to the new melt season. The water table is likely to rise further in the future, as more melt/rain and a denser firn pack are expected in a warmer climate. This may newly induce refreezing of the PFA from above. With continued firn densification, the water table in our study area is likely to locally reach the surface in the coming decades.

Data and code availability

Datasets used as input: the NPI Digital elevation model from (Norwegian Polar Institute, 2014), firn density and meltwater input from the EBFM (Van Pelt et al., 2019). MODLFOW 6 and the adapted python package to generate the configuration files are open-source and freely available, see Bakker et al. (2016); Langevin et al. (2017). LPFAM model data, code and GPR observations available on request.

Author contributions

TvdA designed the LPFAM and tuned it, and performed the main simulation. WvP provided the EBFM input files, and provided feedback and support during the LPFAM modelling. RP refined the GPR data into usable water table depth datasets. VP initiated and coordinates the field work expeditions. TvdA prepared the manuscript, with contributions from all authors.

The authors declare no competing interests.

References

Bakker, M., Post, V., Langevin, C. D., Hughes, J. D., White, J. T., Starn, J., and Fienen, M. N.: Scripting MODFLOW model development using Python and FloPy, Groundwater, 54, 733-739, 2016.

Bintanja, R. and Andry, O.: Towards a rain-dominated Arctic, Nature Climate Change, 7, 263-267, 2017.

Brils, M., Kuipers Munneke, P., van de Berg, W. J., and van den Broeke, M.: Improved representation of the contemporary Greenland ice sheet firn layer by IMAU-FDM v1. 2G, Geoscientific Model Development, 15, 7121-7138, 2022.

Christianson, K., Kohler, J., Alley, R. B., Nuth, C., and Van Pelt, W. J.: Dynamic perennial firn aquifer on an Arctic glacier, Geophysical Research Letters, 42, 1418-1426, 2015.

Flink, A. E., Noormets, R., Kirchner, N., Benn, D. I., Luckman, A., and Lovell, H.: The evolution of a submarine landform record following recent and multiple surges of Tunabreen glacier, Svalbard, Quaternary Science Reviews, 108, 37-50, 2015.

Forster, R. R., Box, J. E., Van Den Broeke, M. R., Miège, C., Burgess, E. W., Van Angelen, J. H., Lenaerts, J. T., Koenig, L. S., Paden, J., and Lewis, C.: Extensive liquid meltwater storage in firn within the Greenland ice sheet, Nature Geoscience, 7, 95-98, 2014.

Fountain, A. G.: The storage of water in, and hydraulic characteristics of, the firn of South Cascade Glacier, Washington State, USA, Annals of Glaciology, 13, 69-75, 1989.

Fountain, A. G. and Walder, J. S.: Water flow through temperate glaciers, Reviews of Geophysics, 36, 299-328, 1998.

425 Gregory, S., Albert, M., and Baker, I.: Impact of physical properties and accumulation rate on pore close-off in layered firn, The Cryosphere, 8, 91-105, 2014.

Haakenstad, H., Breivik, Ø., Reistad, M., and Aarnes, O. J.: NORA10EI: A revised regional atmosphere-wave hindcast for the North Sea, the Norwegian Sea and the Barents Sea, Int. J. Climatol, 40, 4347-4373, 2020.

Haga, O. N., McNabb, R., Nuth, C., Altena, B., Schellenberger, T., and Kääb, A.: From high friction zone to frontal collapse:
430 dynamics of an ongoing tidewater glacier surge, Negribreen, Svalbard, Journal of Glaciology, 66, 742-754, 2020.

Hansen, B. B., Isaksen, K., Benestad, R. E., Kohler, J., Pedersen, Å. Ø., Loe, L. E., Coulson, S. J., Larsen, J. O., and Varpe, Ø.: Warmer and wetter winters: characteristics and implications of an extreme weather event in the High Arctic, Environmental Research Letters, 9, 114021, 2014.

Hawrylak, M.: Surface crevasses on Svalbard: Spatial Distribution Analysis with Focus on the Lomonosovfonna Ice Cap,
435 Uppsala University, 2021.

Hawrylak, M. and Nilsson, E.: Spatial and Temporal Variations in a Perennial Firn Aquifer on Lomonosovfonna, Svalbard, Uppsala Univerisity, 2019.

Herron, M. M. and Langway, C. C.: Firn densification: an empirical model, Journal of Glaciology, 25, 373-385, 1980.

Humphrey, N. F., Harper, J. T., and Meierbachtol, T. W.: Physical limits to meltwater penetration in firn, Journal of Glaciology,
440 67, 952-960, 2021.

Huss, M.: Density assumptions for converting geodetic glacier volume change to mass change, The Cryosphere, 7, 877-887, 2013.

Kingslake, J., Ely, J. C., Das, I., and Bell, R. E.: Widespread movement of meltwater onto and across Antarctic ice shelves, Nature, 544, 349-352, 2017.

445 Koch, M., Seehaus, T., Friedl, P., and Braun, M.: Automated Detection of Glacier Surges from Sentinel-1 Surface Velocity Time Series—An Example from Svalbard, Remote Sensing, 15, 1545, 2023.

Koenig, L. S., Miège, C., Forster, R. R., and Brucker, L.: Initial in situ measurements of perennial meltwater storage in the Greenland firn aquifer, Geophysical Research Letters, 41, 81-85, 2014.

Kuipers Munneke, P., Ligtenberg, S. R., Suder, E. A., and Van den Broeke, M. R.: A model study of the response of dry and
450 wet firn to climate change, Annals of Glaciology, 56, 1-8, 2015.

Kuipers Munneke, P., M. Ligtenberg, S., Van Den Broeke, M., Van Angelen, J., and Forster, R.: Explaining the presence of perennial liquid water bodies in the firn of the Greenland Ice Sheet, Geophysical Research Letters, 41, 476-483, 2014.

Langevin, C. D., Hughes, J. D., Banta, E. R., Niswonger, R. G., Panday, S., and Provost, A. M.: Documentation for the MODFLOW 6 groundwater flow model, US Geological Survey2328-7055, 2017.

455 Lenaerts, J., Lhermitte, S., Drews, R., Ligtenberg, S., Berger, S., Helm, V., Smeets, C., Broeke, M. v. d., Van De Berg, W. J., and Van Meijgaard, E.: Meltwater produced by wind–albedo interaction stored in an East Antarctic ice shelf, Nature climate change, 7, 58-62, 2017.

Lenaerts, J. T., Ligtenberg, S. R., Medley, B., Van de Berg, W. J., Konrad, H., Nicolas, J. P., Van Wessem, J. M., Trusel, L. D., Mulvaney, R., and Tuckwell, R. J.: Climate and surface mass balance of coastal West Antarctica resolved by regional
460 climate modelling, Annals of Glaciology, 59, 29-41, 2018.

Ligtenberg, S., Helsen, M., and Van den Broeke, M.: An improved semi-empirical model for the densification of Antarctic firn, The Cryosphere, 5, 809-819, 2011.

Marchenko, S., Cheng, G., Lötstedt, P., Pohjola, V., Pettersson, R., Van Pelt, W., and Reijmer, C.: Thermal conductivity of firn at Lomonosovfonna, Svalbard, derived from subsurface temperature measurements, The Cryosphere, 13, 1843-1859, 2019.

465 Marchenko, S., Van Pelt, W. J., Claremar, B., Pohjola, V., Pettersson, R., Machguth, H., and Reijmer, C.: Parameterizing deep water percolation improves subsurface temperature simulations by a multilayer firn model, Frontiers in Earth Science, 5, 16, 2017a.

Marchenko, S., Pohjola, V. A., Pettersson, R., Van Pelt, W. J., Vega, C. P., Machguth, H., Bøggild, C. E., and Isaksson, E.: A plot-scale study of firn stratigraphy at Lomonosovfonna, Svalbard, using ice cores, borehole video and GPR surveys in 2012–
470 14, Journal of Glaciology, 63, 67-78, 2017b.

Marchenko, S. A., Van Pelt, W. J., Pettersson, R., Pohjola, V. A., and Reijmer, C. H.: Water content of firn at Lomonosovfonna, Svalbard, derived from subsurface temperature measurements, Journal of Glaciology, 67, 921-932, 2021.

Miller, O., Voss, C. I., Solomon, D. K., Miège, C., Forster, R., Schmerr, N., and Montgomery, L.: Hydrologic modeling of a perennial firn aquifer in southeast Greenland, Journal of Glaciology, 69, 607-622, 2023.

475 Miller, O., Solomon, D. K., Miège, C., Koenig, L., Forster, R., Schmerr, N., Ligtenberg, S. R., Legchenko, A., Voss, C. I., and Montgomery, L.: Hydrology of a perennial firn aquifer in Southeast Greenland: an overview driven by field data, Water Resources Research, 56, e2019WR026348, 2020.

Miller, O. L., Solomon, D. K., Miège, C., Koenig, L. S., Forster, R. R., Montgomery, L. N., Schmerr, N., Ligtenberg, S. R., Legchenko, A., and Brucker, L.: Hydraulic conductivity of a firn aquifer in southeast Greenland, Frontiers in Earth Science, 480 5, 38, 2017.

Nordli, Ø., Wyszyński, P., Gjelten, H., Isaksen, K., Łupikasza, E., Niedźwiedź, T., and Przybylak, R.: Revisiting the extended Svalbard Airport monthly temperature series, and the compiled corresponding daily series 1898–2018, 2020.

Norwegian Polar Institute: Terrengmodell Svalbard (S0 Terrengmodell) [Data set] [dataset], https://doi.org/10.21334/npolar.2014.dce53a47, 2014.

485 Ochwat, N. E., Marshall, S. J., Moorman, B. J., Criscitiello, A. S., and Copland, L.: Evolution of the firn pack of Kaskawulsh Glacier, Yukon: meltwater effects, densification, and the development of a perennial firn aquifer, The Cryosphere, 15, 2021.

Pohjola, V., Moore, J., Isaksson, E., Jauhiainen, T., Van de Wal, R., Martma, T., Meijer, H., and Vaikmäe, R.: Effect of periodic melting on geochemical and isotopic signals in an ice core from Lomonosovfonna, Svalbard, Journal of Geophysical Research: Atmospheres, 107, ACL 1-1-ACL 1-14, 2002.

490 Poinar, K., Joughin, I., Lilien, D., Brucker, L., Kehrl, L., and Nowicki, S.: Drainage of Southeast Greenland firn aquifer water through crevasses to the bed, Frontiers in Earth Science, 5, 5, 2017.

Schaap, T., Roach, M. J., Peters, L. E., Cook, S., Kulessa, B., and Schoof, C.: Englacial drainage structures in an East Antarctic outlet glacier, Journal of Glaciology, 66, 166-174, 2020.

Steger, C. R., Reijmer, C. H., Van Den Broeke, M. R., Wever, N., Forster, R. R., Koenig, L. S., Kuipers Munneke, P., Lehning, 495 M., Lhermitte, S., and Ligtenberg, S. R.: Firn meltwater retention on the Greenland ice sheet: A model comparison, Frontiers in earth science, 5, 3, 2017.

Stevens, C. M., Verjans, V., Lundin, J., Kahle, E. C., Horlings, A. N., Horlings, B. I., and Waddington, E. D.: The community firn model (cfm) v1. 0, Geoscientific Model Development, 13, 4355-4377, 2020.

Stevens, I. T., Irvine-Fynn, T. D., Porter, P. R., Cook, J. M., Edwards, A., Smart, M., Moorman, B. J., Hodson, A. J., and 500 Mitchell, A. C.: Near-surface hydraulic conductivity of northern hemisphere glaciers, Hydrological Processes, 32, 850-865, 2018.

Van de Wal, R. S., Mulvaney, R., Isaksson, E., Moore, J. C., Pinglot, J. F., Pohjola, V. A., and Thomassen, M. P.: Reconstruction of the historical temperature trend from measurements in a medium-length borehole on the Lomonosovfonna plateau, Svalbard, Annals of Glaciology, 35, 371-378, 2002.

505 Van Pelt, W. and Kohler, J.: Modelling the long-term mass balance and firn evolution of glaciers around Kongsfjorden, Svalbard, Journal of Glaciology, 61, 731-744, 2015.

Van Pelt, W., Oerlemans, J., Reijmer, C., Pohjola, V., Pettersson, R., and Van Angelen, J.: Simulating melt, runoff and refreezing on Nordenskiöldbreen, Svalbard, using a coupled snow and energy balance model, The Cryosphere, 6, 641-659, 2012.

510 Van Pelt, W., Oerlemans, J., Reijmer, C., Pettersson, R., Pohjola, V. A., Isaksson, E., and Divine, D.: An iterative inverse method to estimate basal topography and initialize ice flow models, The Cryosphere, 7, 987-1006, 2013.

Van Pelt, W., Pohjola, V., Pettersson, R., Marchenko, S., Kohler, J., Luks, B., Hagen, J. O., Schuler, T. V., Dunse, T., and Noël, B.: A long-term dataset of climatic mass balance, snow conditions, and runoff in Svalbard (1957–2018), The Cryosphere, 13, 2259-2280, 2019.

515 Van Pelt, W. J., Pohjola, V. A., Pettersson, R., Ehwald, L. E., Reijmer, C. H., Boot, W., and Jakobs, C. L.: Dynamic response of a High Arctic glacier to melt and runoff variations, Geophysical Research Letters, 45, 4917-4926, 2018.

van Wessem, J. M., Steger, C. R., Wever, N., and van den Broeke, M. R.: Modelling perennial firn aquifers in the Antarctic Peninsula (1979–2016), The Cryosphere Discussions, 2020, 1-30, 2020.

van Wessem, J. M., Steger, C. R., Wever, N., and van den Broeke, M. R.: An exploratory modelling study of perennial firn 520 aquifers in the Antarctic Peninsula for the period 1979-2016, The Cryosphere, 15, 695-714, 2021.

Vandecrux, B., Mottram, R., Langen, P. L., Fausto, R. S., Olesen, M., Stevens, C. M., Verjans, V., Leeson, A., Ligtenberg, S., and Kuipers Munneke, P.: The firn meltwater Retention Model Intercomparison Project (RetMIP): evaluation of nine firn models at four weather station sites on the Greenland ice sheet, The Cryosphere Discussions, 2020, 1-32, 2020.

525   Veldhuijsen, S., van de Berg, W. J., Munneke, P. K., Hansen, N., Boberg, F., and van den Broeke, M.: Exploring the future expansion of perennial firn aquifers in Antarctica using a random forest emulator, Copernicus Meetings, 2024.

Veldhuijsen, S. B., van de Berg, W. J., Kuipers Munneke, P., and van den Broeke, M. R.: Evolution of Antarctic firn air content under three future warming scenarios, EGUsphere, 2023, 1-27, 2023.